Flat bands and ferrimagnetic order in electronically correlated dice-lattice ribbons

Rahul Soni [1,2] Nitin Kaushal,[1,2] Satoshi Okamoto [2] and Elbio Dagotto[1,2]

[1]*Department of Physics and Astronomy, The University of Tennessee, Knoxville, Tennessee 37996, USA*
[2]*Materials Science and Technology Division, Oak Ridge National Laboratory, Oak Ridge, Tennessee 37831, USA*

We study ribbons of the dice two-dimensional lattice (that we call "dice ladders") known to have nontrivial topological properties, such as Chern numbers 2 [Wang and Ran, Phys. Rev. B **84**, 241103(R) (2011)]. Our main results are two fold. (1) Analyzing the tight-binding model in the presence of Rashba spin-orbit coupling and an external magnetic field, we observed that dice ladders qualitatively display properties similar to their two-dimensional counterpart all the way to the limit of only two legs in the short direction. This includes flat bands near the Fermi level, edge currents and edge charge localization near zero energy when open boundary conditions are used, two chiral edge modes, and a nonzero Hall conductance. (2) We studied the effect of Hubbard correlation U in the two-leg dice ladder using Lanczos and density matrix renormalization group techniques. We show that by increasing U the flat bands split without the need of introducing external fields. Moreover, robust ferrimagnetic order develops. Overall, our work establishes dice ladders as a promising playground to study the combined effect of topology and correlation effects, one of the frontiers in quantum materials.

I. INTRODUCTION AND DICE LATTICE

In his seminal paper, Haldane proposed a tight-binding model on a honeycomb lattice, including a staggered flux pattern, that displays the integer quantum Hall effect [1]. Time-reversal symmetry is broken by the complex-valued second-neighbor hoppings and no external magnetic fields are needed. Generalizations led to the concept of topological insulators [2–4]. Later, it was discovered that a similar approach worked even for the fractional quantum Hall effect, also without employing Landau levels and large magnetic fields [5–9]. The essence is to search for models that display quasi-two-dimensional flat bands with a nonzero Chern number. The topological band structures created by this procedure are of considerable current interest. These types of models are referred to as lattice Chern insulators. The Chern number equals the number of chiral edge modes.

The two-dimensional Haldane model involving two triangular lattices was generalized to three by Wang and Ran [10] (see also Ref. [11]). By this procedure fine-tuning of parameters is avoided, and the honeycomb lattice becomes the *dice* lattice [12–14], Fig. 1, via the addition of an extra site at the center of each hexagon. This bipartite lattice has two types of sites: two-thirds with coordination three and one-third with coordination six. The unit cell contains three sites, thus leading to three bands. At the noninteracting tight-binding level and with a small Zeeman field—with hoppings only between nearest-neighbor sites and including Rashba spin-orbit coupling λ—the model displays bands with Chern number $C = 2$ [15], as opposed to the more standard $C = 1$ of Landau levels in the integer quantum Hall effect.

The dice lattice could be realized in cold atoms or via a trilayer superlattice grown in the [111] direction [16], such as in $SrTiO_3/SrIrO_3/SrTiO_3$. From the theory perspective, the α-T_3 model, interpolating between the honeycomb and dice lattices, also received considerable attention [17–20]. In dice lattices, the effect of interactions was considered using weak coupling and mean-field techniques [21]. Its realization in optical lattices [22,23] and in $LaAlO_3/SrTiO_3$ (111) quantum wells [24] was also studied. Bulk oxides with the generic formula $A_4B'B_2O_{12}$, such as $Ba_4CoRe_2O_{12}$ [25], contain trilayers that seen "from above" also resemble a dice lattice.

In this paper, we study ribbons of the dice lattice. This is equivalent to a dimensional reduction from two to one of the original dice lattice into a quasi-one-dimensional system, conceptually similar to studying graphene in two dimensions versus carbon nanotubes in one dimension: locally the atomic connections are the same, but globally both systems are different. Graphene nanoribbons were also studied in recent efforts [26]. We refer to the dice ribbons as "dice ladders" borrowing the language of correlated electronic systems: the dice lattice is two-dimensional, while the dice ladder is one-dimensional, with a finite length in the short direction. We use three primary boundary conditions: (i) cylindrical geometry, with periodic boundary conditions (PBC) in the short direction and open boundary conditions (OBC) in the long one, or vice versa; (ii) torus geometry, with PBC in both directions; (iii) open geometry, with OBC in both directions (i.e., sharp edges). The last is important to visualize in real space the edge currents and edge charge localization. Twisted boundary conditions and the associated average over many edge angles were not used because such a procedure would be too demanding in CPU time when including a Hubbard U. Because the dice lattice has a complicated geometry, and the unit cell has three sites, for the benefit of the reader the case of a 3×2 unit-cells cluster with the three boundary conditions used in our work is illustrated in Fig. 2. Note that this cluster has a total of 18 sites. Also, to avoid confusion with alternative conventions used in Mesoscopic physics, note that we follow the notation of correlated electrons where "open boundary
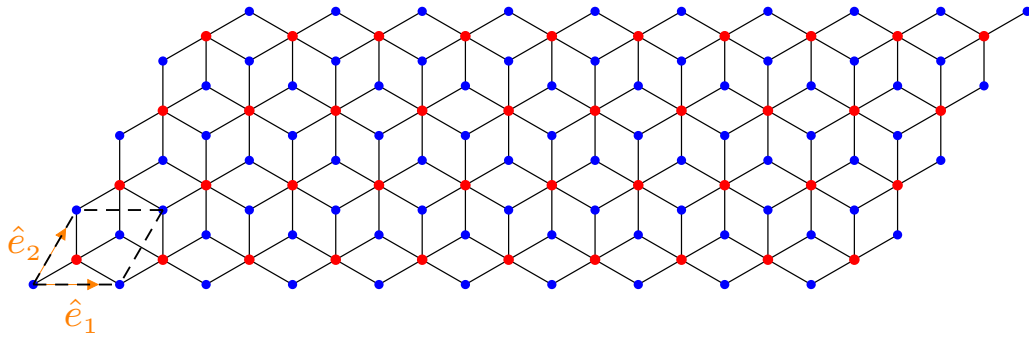
FIG. 1. Dice lattice geometry. Blue dots are sites with coordination number 3, while red dots have coordination number 6. The dashed black box describes the unit cell of the lattice. $\hat{e}_1$ and $\hat{e}_2$ (in orange) are the lattice unit vectors. Specifically, here we show a 10×4 lattice with ten unit cells along the $\hat{e}_1$ and 4 unit cells along the $\hat{e}_2$ directions (simply count the number of red dots).

conditions" means that the system ends abruptly at the edge. "Open" here is not used in the sense of connected to, for example, leads.

Our effort has unveiled two primary results. (1) Dice ladders, i.e., dice ribbons, keep their primary properties even in the smallest dice ladder we studied. (2) Exploiting this result, numerically we introduced correlation Hubbard U effects and found that ferrimagnetic order develops with increasing U. More specifically we found the following.

(1) Using the three boundary conditions described above, we unveiled a rich eigenvalue spectrum that, surprisingly, continues displaying flat bands even into the smallest ladders we studied. In principle, flat bands originate in localized states and reducing one dimension should have minor consequences until the natural localization length scale is reached. What is interesting of our results is that the flat bands survive even for the smallest ladder we studied, the $N \times 2$ ladder. It was not possible to anticipate *a priori* that such a thin system would still have flat bands. In addition, all the geometries studied here display a nonzero Hall conductance in the flat bands region, with the particular value of the 4-leg ladder system at the Fermi level being very close to $C = 2$ as in the planar dice lattice. Moreover, edge currents and edge charge localization appear in all the ladders near zero energy, even

in the smallest $N \times 2$ cluster, when using both OBC $\times$ OBC and PBC $\times$ OBC. Thus, even the smallest dice ladder studied here displays properties that resemble the two-dimensional topologically nontrivial system [27,28]. Note that sharp topological numbers, such as integer Chern numbers, cannot be obtained using dice ladders because of the finite number of momenta in the short direction when using cylindrical or fully periodic boundary conditions that prevents a smooth definition of the momentum derivatives involved in the integral that defines C. However, we will show that all properties of the quasi-one-dimensional dice ladders are qualitatively similar to those of the truly topological two-dimensional systems, and in these regards, dice ladders are useful "toy models" for dice planes. Their primary importance lies in the fact that correlation effects can be accurately introduced computationally in $N \times 2$ ladders but not in planar geometries.

(2) The influence of correlation effects on topological systems [29] is an important open problem that can be studied in dice ladders. In particular, here in the $N \times 2$ ladder we incorporated Hubbard U repulsion via powerful unbiased numerical techniques beyond mean-field approximations, such as the Lanczos [30] and density matrix renormalization group (DMRG) methods [31]. Below we show that as U increases, ferrimagnetic order develops, in agreement with spin-1/2

(a)   (b)   (c)
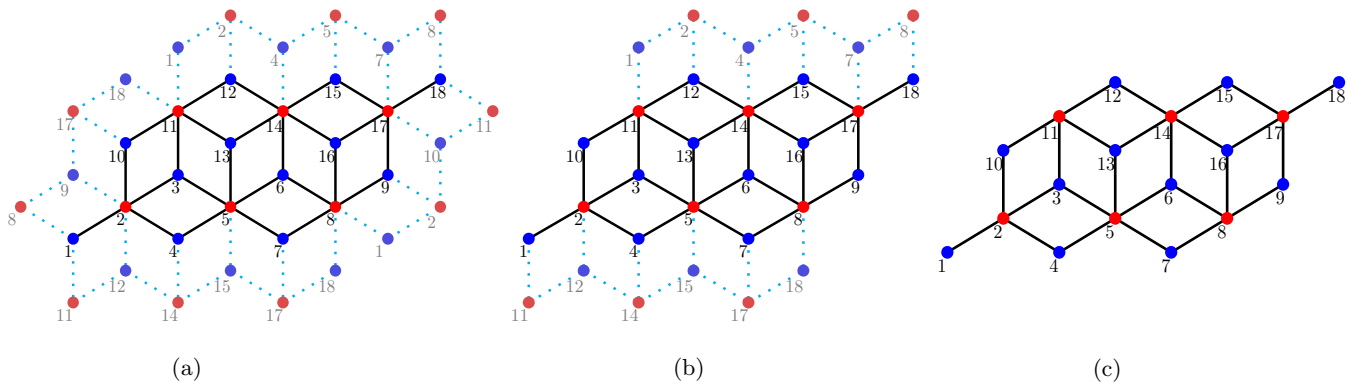
FIG. 2. Boundary conditions used in our study, employing a 3×2 unit-cells cluster as example. Each unit cell has three sites, thus there are 18 sites in this cluster. Panel (a) corresponds to PBC $\times$ PBC, i.e., periodic boundary conditions in both directions. The specific neighbors of each site at the boundary are labeled by site numbers. The solid (dashed) lines denote connections inside the cluster (across the boundary). (b) Similar as (a) but with PBC along the vertical direction and OBC along the horizontal direction. (c) Similar to (a) but using open boundary conditions in both directions. Here "open" refers to a sharp edge, as opposed to connection to leads or reservoirs.

Heisenberg model calculations [32]. Moreover, the original $U = 0$ flat bands split due to the magnetic order that emerges. Then, for this split to occur external magnetic fields are not needed. Our results prove that dice ladders can be studied numerically with accuracy even with nonzero U and opens several avenues of future investigation. How are the edge states affected by U? What is the complete phase diagram in the plane U-λ? Are there new phases?

This path of future research resembles the successful strategy followed in cuprates and pnictides/selenides superconductors where also the two-dimensional original problem was transformed to the geometry of N-leg ladders to allow for computational accuracy. In particular, recent experimental and theoretical work showed that real two-leg ladder iron-based materials, such as $BaFe_2S_3$ [33,34], turn superconducting with high pressure and display nontrivial magnetic properties [35–37]. In Cu-oxide ladders, similar success was theoretically and experimentally achieved [38–40]. Exploring the physics of interacting N-leg dice ladders can define an equally fertile area of research.

The organization of the paper is as follows. In Sec. II, the model and methodology used will be introduced, as well as the main observables calculated. Section III contains the main numerical results for the tight-binding model reduction from planes to ladders. We study the density-of-states (DOS) and flat bands, starting with the $N \times N$ cluster, followed by the $N \times 4$ ladder, and then the $N \times 3$ and $N \times 2$ ladders. Section IV addresses the edge currents, edge charge localization, and Hall conductance, still within the noninteracting tight-binding model. Section V presents our results incorporating Hubbard U correlations for the $N \times 2$ case, focusing on the ferrimagnetic order that develops and on the splitting of the flat bands even without magnetic fields. Conclusions are in Sec. VI.

II. MODELS AND METHODS

A. Hamiltonian

In Sec. III and IV of this paper, we will consider the same noninteracting Hamiltonian studied in Ref. [10]. In this previous work, a two-dimensional geometry was used while here we use a ribbon geometry. This tight-binding Hamiltonian has three components: $H = H_K + H_{SOC} + H_B$, where H_K is the tight-binding kinetic energy, H_{SOC} is the Rashba spin-orbit coupling (SOC), and H_B the interaction of electrons with an external magnetic field. The kinetic term H_K is defined as

$$H_K = -t \sum_{\substack{\mathbf{r}, \alpha, \mathbf{r}', \beta \\ \sigma}} (c^\dagger_{\mathbf{r},\alpha,\sigma} c_{\mathbf{r}',\beta,\sigma} + \text{H.c.}) - \epsilon \sum_{\mathbf{r}} n_{\mathbf{r},2}, \quad (1)$$

where $\mathbf{r}, \mathbf{r}'$ are the unit cell indexes [$\mathbf{r} = (r_1, r_2)$ is a vector with components in a coordinate system defined using the unit vectors in Fig. 1], α and β are the site indexes within the unit cell $\mathbf{r}$ and $\mathbf{r}'$, respectively (with $\alpha, \beta = 1, 2, 3$), and $\sigma = \uparrow, \downarrow$ is the z-axis spin projection of the electron at site α within the unit cell $\mathbf{r}$. The on-site energy is ϵ and $n_{\mathbf{r},\alpha} = \sum_\sigma c^\dagger_{\mathbf{r},\alpha,\sigma} c_{\mathbf{r},\alpha,\sigma}$ is the local density of electrons at site α in the unit cell $\mathbf{r}$. ϵ affects only the "red" sites of Fig. 1 (those with coordination 6). This kinetic term depicts the inter- or

intra-unit cell electronic tunneling between nearest-neighbor lattice sites $\mathbf{r}, \alpha$ and $\mathbf{r}', \beta$ with hopping amplitude t. In this article, t is the energy unit. The electronic density is half-filling, i.e., one electron per site. The actual value of the lattice parameter is not important in our qualitative study.

While, in principle, a gauge field in the hopping term should be added once magnetic fields are included, the effects we focus on occur even for very small fields. It would be confusing to the readers to alter simultaneously the geometry and the Hamiltonian of the dice model [10]. Thus, including gauge fields is postponed for when concrete physical realizations of dice planes or ladders are experimentally studied in materials or cold atoms.

The Rashba-SOC term in the Hamiltonian is

$$H_{SOC} = -\lambda \sum_{\substack{\mathbf{r}, \mathbf{r}', \\ \alpha, \beta, \sigma, \sigma'}} [\mathrm{i} c^\dagger_{\mathbf{r},\alpha,\sigma} (\hat{D}_{\alpha\beta} . \vec{\tau})_{\sigma\sigma'} c_{\mathbf{r}',\beta,\sigma'} + \text{H.c.}], \quad (2)$$

where i is the imaginary unit, $\vec{\tau} = \tau_x \hat{x} + \tau_y \hat{y} + \tau_z \hat{z}$ is the Pauli matrix vector, $\hat{D}_{\alpha\beta}$ is the unit vector in-plane and perpendicular to the bond formed by $(\mathbf{r}, \alpha)$ and $(\mathbf{r}', \beta)$ (see illustration in Appendix A). The hopping is only between nearest-neighbor sites.

The last term of the tight-binding Hamiltonian is the interaction of the spin of electrons with a magnetic field

$$H_B = -B \sum_{\mathbf{r},\alpha,\sigma,\sigma'} \tau^z_{\sigma\sigma'} c^\dagger_{\mathbf{r},\alpha,\sigma} c_{\mathbf{r},\alpha,\sigma'}, \quad (3)$$

where B is the strength of the magnetic field perpendicular to the plane of the lattice along the z-direction. This magnetic term breaks time-reversal. The Hamiltonian still has translational invariance. For typical oxides the hopping t is approximately 0.1 eV, and thus the magnetic field used here of value $0.2t$, as in Ref. [10], is large. However, the flat band split found in Ref. [10] and here occurs for much smaller magnetic fields. Thus, $B = 0.2t$ is only used for clarity in the visualization of results. The physics does not change if much smaller fields are used.

In momentum space, the noninteracting Hamiltonian becomes

$$H(\mathbf{k})$$
$$= \begin{pmatrix} -B & 0 & -t\gamma^*_{\mathbf{k}} & -\mathrm{i}\lambda\gamma^*_{\mathbf{k}+} & 0 & 0 \\ 0 & B & -\mathrm{i}\lambda\gamma^*_{\mathbf{k}-} & -t\gamma^*_{\mathbf{k}} & 0 & 0 \\ -t\gamma_{\mathbf{k}} & \mathrm{i}\lambda\gamma_{\mathbf{k}-} & -\epsilon-B & 0 & -t\gamma^*_{\mathbf{k}} & \mathrm{i}\lambda\gamma^*_{\mathbf{k}+} \\ \mathrm{i}\lambda\gamma_{\mathbf{k}+} & -t\gamma_{\mathbf{k}} & 0 & -\epsilon+B & \mathrm{i}\lambda\gamma^*_{\mathbf{k}-} & -t\gamma^*_{\mathbf{k}} \\ 0 & 0 & -t\gamma_{\mathbf{k}} & -\mathrm{i}\lambda\gamma_{\mathbf{k}-} & -B & 0 \\ 0 & 0 & -\mathrm{i}\lambda\gamma_{\mathbf{k}+} & -t\gamma_{\mathbf{k}} & 0 & B \end{pmatrix}$$
$$(4)$$

after the Fourier transform $c^\dagger_{\mathbf{k},\alpha,\sigma} = \frac{1}{\sqrt{3NM}} \sum_{\mathbf{r}} e^{\mathrm{i}\mathbf{k}.\mathbf{r}} c^\dagger_{\mathbf{r},\alpha,\sigma}$ is used, with N (M) the number of points in the long (short) direction. We defined $\gamma_{\mathbf{k}} = 1 + e^{\mathrm{i}k_1} + e^{\mathrm{i}k_2}$, and $\gamma_{\mathbf{k}\pm} = 1 + e^{\mathrm{i}(k_1 \pm 2\pi/3)} + e^{\mathrm{i}(k_2 \pm 4\pi/3)}$, where the components are along the axes indicated in Fig. 1 as $k_i = \mathbf{k} \cdot \hat{e}_i$. The annihilation operator basis is $(c_{\mathbf{k},1,\uparrow}, c_{\mathbf{k},1,\downarrow}, c_{\mathbf{k},2,\uparrow}, c_{\mathbf{k},2,\downarrow}, c_{\mathbf{k},3,\uparrow}, c_{\mathbf{k},3,\downarrow})$. This matrix can be diagonalized and the results are in Fig. 3: 3(a) at $\lambda = 0$ and $B = 0$, there are three bands, with one
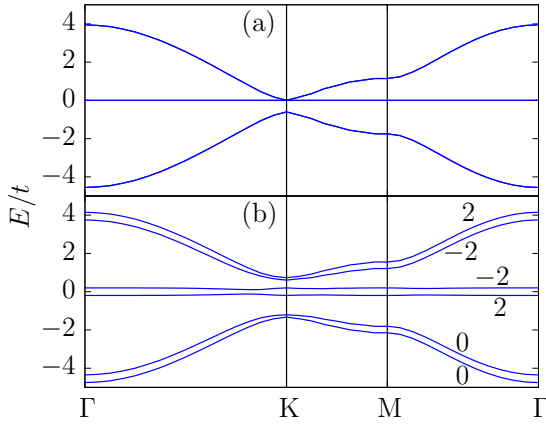
FIG. 3. Energy bands for the $N \times N$ dice lattice obtained diagonalizing the 6×6 Hamiltonian matrix Eq. (4) in momentum space. Panel (a) are results for $\lambda = B = 0$, while (b) are for $\lambda = 0.3t$ and $B = 0.2t$. In both cases, $\epsilon = 0.6t$. These bands, already shown in [10], are reproduced here for the benefit of the reader.

totally flat and touching another at the K point [10]; 3(b) with nonzero λ and B the original three bands split into six, with the Chern numbers (definition in Appendix B) as indicated.

In this first numerical investigation of electronic correlation effects on dice ladders, as described in Sec. V, we also introduce the repulsive Hubbard interaction term which reads as

$$H_U = U \sum_{\mathbf{r},\alpha} n_{\mathbf{r},\alpha,\uparrow} n_{\mathbf{r},\alpha,\downarrow}, \tag{5}$$

where U is the strength of the Hubbard interaction, and the number operator is $n_{\mathbf{r},\alpha,\sigma} = c^\dagger_{\mathbf{r},\alpha,\sigma} c_{\mathbf{r},\alpha,\sigma}$.

B. Observables calculated

1. Currents

The charge current operators are defined as the sum of two terms, J^K_{ij} and J^{SO}_{ij}, known as the spin preserving and spin flipping currents, respectively [41]. The first has a canonical form and arises from the kinetic energy term, while the second originates in the Rashba term and vanishes if $\lambda = 0$. We followed the local conservation of charge current to derive these operators. Some details of the calculation of these charge current operators are in Appendix A and in Ref. [41].

2. Hall conductance

From the currents, we computed the transverse Hall conductance (σ_{xy}), described by the Kubo formula as recently studied by the authors of Ref. [42]:

$$\sigma_{xy} = \frac{2\pi}{N_s} \sum_{\varepsilon_m \neq \varepsilon_n} \frac{f_m - f_n}{\zeta^2 + (\varepsilon_n - \varepsilon_m)^2} \mathrm{Im}\big(J_{\hat{e}_1 mn} J_{\hat{e}_2 nm}\big), \tag{6}$$

where $J_{\hat{e}_1}$ and $J_{\hat{e}_2}$ are the current operators calculated along the lattice vectors $\hat{e}_1$ and $\hat{e}_2$, respectively. $J_{\hat{e}_i mn} = \langle m | J_{\hat{e}_i} | n \rangle$ is the mn^{th} matrix element of the current operator $J_{\hat{e}_i} = J^K_{\hat{e}_i} + J^{SO}_{\hat{e}_i}$. $N_s = 3MN$ is the total number of sites, and $f_m = (1 + e^{-\beta(\epsilon_m - \mu)})^{-1}$ is the Fermi function. ζ is the relaxation parameter introduced to smooth the set of delta functions that

arises from finite-size clusters, and to crudely represent the effects not included in the model, such as lattice fluctuations. $|n\rangle$ refers to the eigenstates of the full Hamiltonian, which in most of the calculations below will be in a real-space basis.

3. Spectral function

The one-particle spectral function used in our calculation employs only momenta along the axis 1 that will remain "long" in our ladders, while axis 2 will be shortened. Specifically, we use the formula

$$A(k_1, \omega) = \frac{1}{N} \sum_{\substack{r_1, r'_1, \\ r_2, \alpha, \sigma}} \sum_m e^{ik_1(r'_1 - r_1)}$$

$$\times \Psi^*_m(r_1, r_2, \alpha, \sigma) \Psi_m(r'_1, r_2, \alpha, \sigma) \delta(\omega - E_m), \tag{7}$$

where r_1 (r_2), r'_1 are the unit cell indices along the lattice vector $\hat{e}_1$ ($\hat{e}_2$). Here, $k_1 = \frac{2\pi n_1}{N}$ is the momentum along $\hat{e}_1$, where $n_1 = 0, \ldots, N - 1$, and N is the number of sites along the long direction of our ladders. m is the eigenvector index with energy E_m, and we define the amplitude $\Psi_m(r_1, r_2, \alpha, \sigma) = \langle r_1, r_2, \alpha, \sigma | m \rangle$. We provide width to the delta functions $\delta(\omega - E_n)$ via a Lorentzian function $\frac{1}{\pi} \frac{1}{(\omega - E_m)^2 + \eta^2}$, with η the broadening of this function. η simulates effects not considered in the model, such as disorder, lattice fluctuations, and temperature, and also allows for a better visualization (smoothing) of results that otherwise would consist of sharp δ functions using a finite cluster. Broadening was also used in our recent study of the skyrmion lattice [42].

4. Spin correlation

To understand the ground-state properties of the Hamiltonian in the presence of interaction at half-filling, we calculated the real-space spin-spin correlation function between two sites $\langle \mathbf{S}_i . \mathbf{S}_j \rangle = \langle S^z_i S^z_j \rangle + \frac{1}{2}(\langle S^-_i S^+_j \rangle + \langle S^+_i S^-_j \rangle)$. These spin correlations were computed via both Lanczos and DMRG techniques. For Lanczos, we used the 2×2 (i.e., 12-sites) cluster. Since the total z-component spin S^z_{Total} is not a good quantum number due to the Rashba-SOC term in the Hamiltonian, the Hilbert-space dimension for our case at half-filling was $^{24}C_{12} = 2.704156 \times 10^6$ states. Meanwhile, the DMRG calculation was performed on the 8×2 ladder system, using a maximum of 1000 states. The truncation error in the calculation of the ground state was $\sim 10^{-7}$.

III. RESULTS

A. $N \times N$ system

We start with a cluster resembling the two-dimensional system but being finite in both directions. This provides a test that working on a finite cluster can properly reproduce the results for the bulk dice lattice [10]. We first study the eigenvalues obtained by discretizing momentum space, as it occurs for a finite system, and later we move into real-space perspectives and calculations of relevance for this problem, such as edge currents.

In Fig. 4(a), we show a small typical two-dimensional dice cluster. The dangling sites shown have indeed such a character
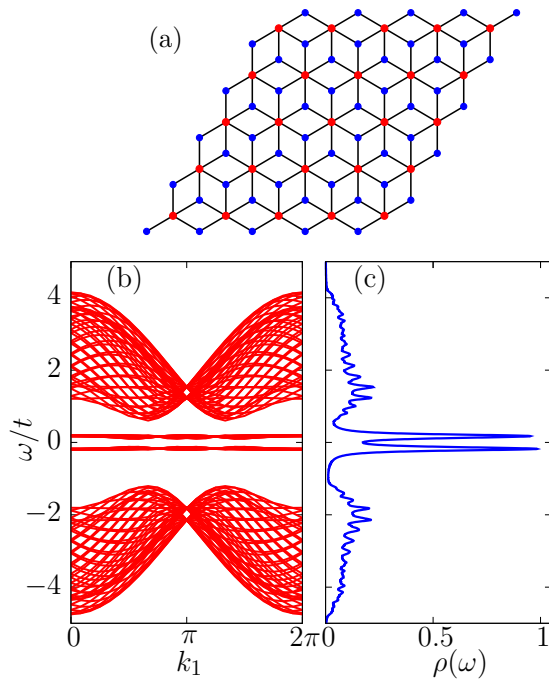
FIG. 4. (a) Sketch of an $N \times N$ cluster. In this illustration N is 5 (focus on the red sites to count unit cells). (b) Bands derived from a 24×24 cluster (PBC $\times$ PBC) using Eq. (4), at $\lambda = 0.3t$ and $B = 0.2t$. Shown are 24×6 bands, with the 6 arising from the product of three sites in the unit cell and a factor of 2 produced by the magnetic field split. Each band has 24 points, joined by interpolating lines. (c) DOS derived from (b) by summing over k_1. Note the sharp peaks near zero energy associated with near flat bands in the DOS, as it occurs in the bulk system in Fig. 3(b). The other dispersive bands are associated with the upper and lower bands in Figs. 3(a) and 3(b).

(singular points) when OBC are used, but for PBC in both directions all sites are equivalent, i.e., blue and red dots have the same connectivity all over the lattice for PBC $\times$ PBC.

In Fig. 4(b), a 24×24 cluster is diagonalized. We use the perspective of the direction "1" which will become the "long" (or leg) direction for dice ladders. Thus, in Fig. 4(b) 24×6 bands are shown, see caption. The DOS is in Fig. 4(c). The results are remarkably close to those implied from Fig. 3(b), particularly with regards to the crucial two flat bands near zero energy. In the DOS upper and lower dispersing bands, only small spikes are the remnants of the finite-size cluster used. In summary, a 24×24 PBC $\times$ PBC cluster is sufficient to capture the essence of the dice lattice, as will also be shown below with regards to several quantities.

B. $N \times 4$ ladder

Consider now a dice ladder with four unit-cells along the short direction, as sketched in Fig. 5(a). Note that because we have a unit cell with three sites, effectively there are 12 lines of sites, with a vertical periodicity blue-blue-red. This shows that numerically the effort to study these ladders after adding electronic interactions U is harder than the nominal size suggests. Specifically, a $N \times 4$ dice ladder demands an effort similar to a $N \times 12$ one-orbital Hubbard model ladder from the DMRG perspective.
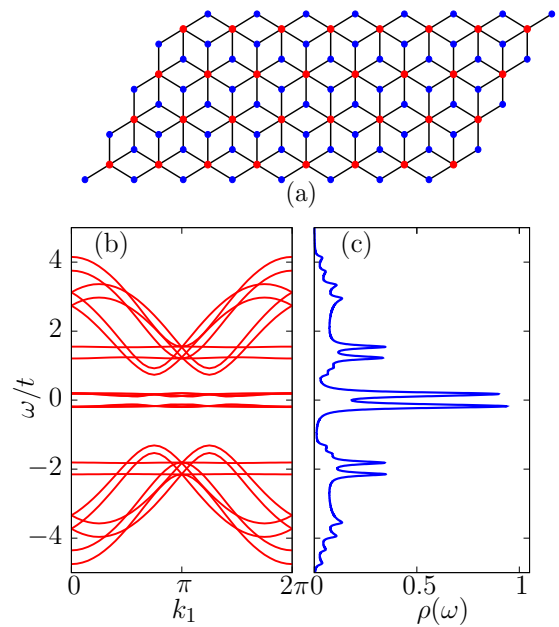

FIG. 5. (a) Sketch of an $N \times 4$ ladder with $N = 8$ (focus on the red sites to count unit cells). (b) Bands derived from a 150×4 cluster (PBC $\times$ PBC) diagonalizing Eq. (4) at $\lambda = 0.3t$ and $B = 0.2t$. Shown are $4 \times 6 = 24$ bands, with the factor 6 explained in the caption of Fig. 4. (c) DOS derived from (b) by summing over k_1. Note the six sharp peaks associated with near flat bands, two of which are isolated near zero energy (the important ones), while four are mixed with other nonflat bands.

With regards to the relevance of dice ladders to mimic planes, what is interesting are the results in Figs. 5(b) and 5(c). In spite of the very different lengths in both directions, Figs. 5(b) and 5(c) are similar to Figs. 4(b) and 4(c). In particular, both display almost identical flat bands near zero energy. To the extent that one of the primary nontrivial aspect of dice lattices are the flat bands, then the $N \times 4$ ladder keeps that aspect intact. In addition, surprisingly, there are other flat bands in this 4-leg ladder, two in the original upper-energy dispersing region and two in the lower-energy region. However, these bands are not isolated from the rest, even with a nonzero λ and B. Thus, their value in inducing nontrivial properties of the system are questionable. For this reason, we will not focus on those extra flat bands. However, we found flat bands near zero energy, successfully confirming that a 4-leg dice ladder resembles the two-dimensional system.

Moreover, following the procedure outlined in the Appendix based on Ref. [43] we calculated the Chern number of the near-zero energy flat bands of the 4-leg dice ladder. In principle, ladders are not expected to have sharp topological properties because of their finite nature in one direction. However, remarkably, we found $C \sim 2$ and $C \sim -2$ for the two flat bands as in Fig. 3(b). For details, see below and Appendix B. In essence, the $N \times 4$ ladder has basically the same properties as the two-dimensional dice lattice.

C. $N \times 3$ system

Consider now dice ladders of size $N \times 3$, as in Fig. 6(a). Here, the effective number of "legs" of the 3-leg dice
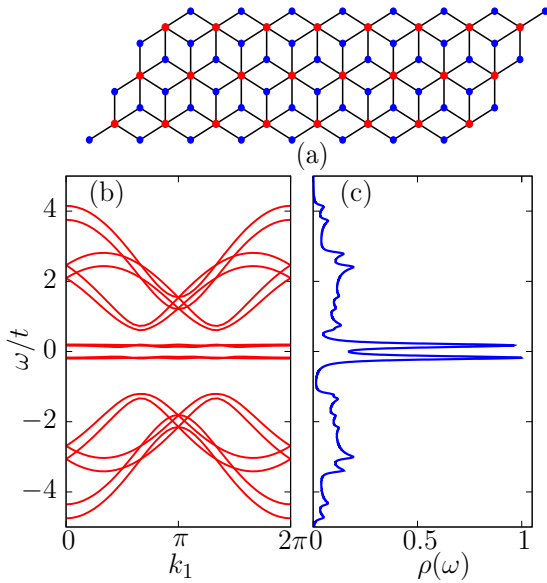
FIG. 6. (a) Sketch of an $N \times 3$ ladder. In the example shown N is 8 (focus on the red sites to count unit cells). (b) Bands derived from a 150×3 cluster (PBC $\times$ PBC) diagonalizing Eq. (4) at $\lambda = 0.3t$ and $B = 0.2t$. Shown are 18 bands, i.e., 3×6, as explained in the caption of Fig. 4. (c) DOS derived from (b) by summing over k_1, clearly displaying flat bands near zero energy.
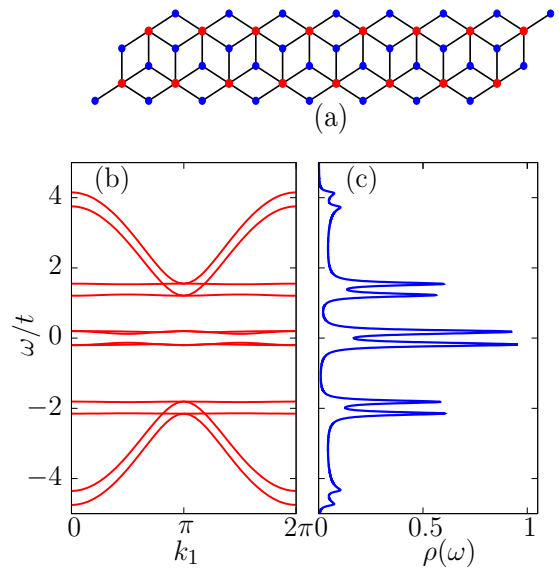

FIG. 7. (a) Sketch of an $N \times 2$ ladder. In the example shown N is 8 (focus on the red sites to count unit cells). (b) Bands derived from a 150×2 cluster (PBC $\times$ PBC) diagonalizing Eq. (4) at $\lambda = 0.3t$ and $B = 0.2t$. Shown are 12 bands, i.e., 2×6, as explained in the caption of Fig. 4. (c) DOS derived from (b) by summing over k_1. Note the six sharp peaks in the DOS associated with near flat bands, two of which are isolated near zero energy, while four are mixed with other nonflat bands.

ladder, of relevance for computational work in real-space when adding Hubbard U, is 9 because each unit cell has three sites. As for the 4-leg ladder, in Fig. 6(b) we present momentum-space results using k_1 in the horizontal axis (long direction). This provides a discrete set of bands because of the finite number of unit cells along the short direction (see caption). Once again, the flat bands near $E = 0$ remain solidly in place. The DOS is still qualitatively similar to the two-dimensional dice lattice cluster Fig. 4(c). In this case, there are no extra flat bands besides those close to Fermi energy zero, contrary to 4-legs, suggesting that the existence of these extra features may depend on whether we have an even or odd number of unit cells along the short direction.

D. $N \times 2$ system

Finally, we arrived to the "shortest" ribbon studied here: the 2-legs dice ladder. This system, when considered in terms of the number of legs along the short direction, has six legs in the one-orbital Hubbard analog, as illustrated in Fig. 7(a). Thus, this system is accessible to present computational efforts using DMRG. For this reason, the 2-leg ladder is particularly important.

In Fig. 7(b) the bands plotted versus k_1 are shown, as before for 3- and 4-leg ladders. Once again, the flat bands near energy zero are clearly present, even in this "shortest" system studied here. Similarly as with four legs, extra flat bands were identified immersed in the upper- and lower-energy regions, but they are not of our interest. The DOS in Fig. 7(c) now are different from the two-dimensional cluster Fig. 4(c) with regards to the upper- and lower-energy regions due to the extra flat bands. But with regards to the region near zero energy, all

systems $N \times N$, $N \times 4$, $N \times 3$, and $N \times 2$, behave similarly: they all have similar flat bands in this energy region.

IV. EDGE CURRENTS AND EDGE STATES

A. Cylindrical boundary conditions

To study the properties of the $U = 0$ dice ladders we performed several other calculations besides the DOS and their flat bands. For example, using *cylindrical* boundary conditions, PBC along the short direction and OBC along the long direction, we searched for edge currents at the edges of this geometry. The results are in Fig. 8. At the center of the cylinders—away from the edges—there are no currents as expected, but at the edges currents develop with opposite senses of circulation. There is a clear similarity, both qualitatively and quantitatively, between the $N \times N$ cluster that mimics the two-dimensional plane, Fig. 8(a), and the dice ribbons in Figs. 8(b), 8(c) and 8(d): they all behave similarly, with edge currents circulating in the same direction and of the same magnitude. Thus, the edge currents of two-dimensional dice lattices in cylinders also appear in the dice ladders.

Using cylindrical boundary conditions creates in-gap states in between the flat bands, whose gap was opened by B. Studying the wave function of those in-gap states, we calculated the electronic density with results also in Fig. 8. As expected, these in-gap states are indeed edge states, associated with the edge currents.

In Fig. 9, we show bands obtained from the one-particle spectral function $A(k_1, \omega)$ (technical aspects in observables Sec. II B) for PBC $\times$ OBC, where the long direction has PBC. We focus on the energy range where the flat bands
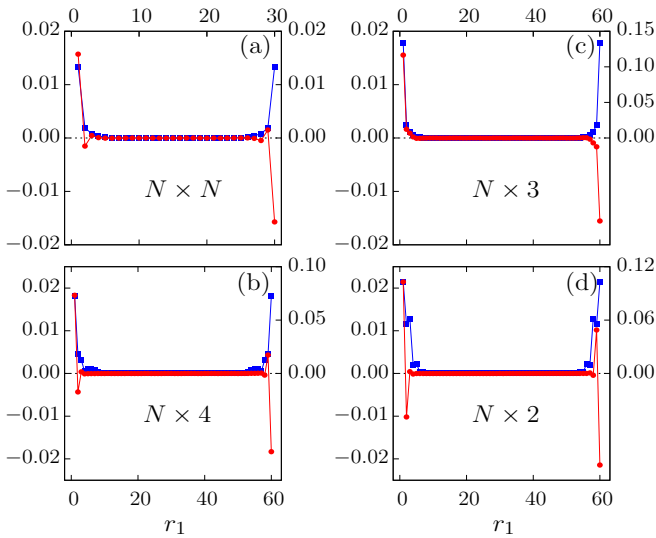
FIG. 8. Charge current $\langle J_{\hat{e}_2} \rangle$ (red dots, left axes) in an OBC $\times$ PBC system shown vs the unit cell index r_1 along the long axis $\hat{e}_1$, for different dice ladders. Electronic density (blue dots, right axes) corresponding to the in-gap states, i.e., states between the two flat bands near zero, with the gap among them generated by the magnetic field. These in-gap states are induced by using cylindrical boundary conditions. The density result is an average over the four in-gap states closest to zero energy. The location of both current and charge suggests these in-gap states are edge states. Shown are averages over the short direction r_2 (in cylindrical geometries the results are translationally invariant along this PBC direction). Panels (a), (b), (c), and (d) are for ladder sizes 30 $\times$ 30, 60 $\times$ 4, 60 $\times$ 3, and 60 $\times$ 2, respectively. Parameters used in all panels are $\lambda = 0.3t$, $B = 0.2t$, $\epsilon = 0.6t$.

develop near zero energy. For PBC $\times$ PBC, these figures simply display two nearly flat bands with no extra features due to the absence of edges. But with PBC $\times$ OBC in our finite but large clusters we observe the development of edge states that manifest as crossing points. The similarity between the $N \times N$ cluster [Fig. 9(a)] and all the rest of the ladders [Figs. 9(b), 9(c) and 9(d)] is clear. In all cases, the presence of two crossing points in principle indicates Chern number $C = 2$. As explained before, for the dice ladders we do not expect a perfect quantization to an integer of the Chern number calculation due to the few momentum-space points available along the short direction. However, the conclusion that all cases in Figs. 9(a) to 9(d) share similar features is clear. All these results suggest that two chiral edge states exist both in the two- and one-dimensional dice systems, even though C is not quantized for ladders.

For completeness, and as with the edge states for cylinders, note that for the 3- and 2-legs dice ladders using other sets of λ and B parameters, we found that a small gap opens at zero energy where the crossings appear in Figs. 9(c) and 9(d) (for 4-legs these gaps are negligible). In the presence of those gaps, edge states were nevertheless observed for 3- and 2-legs suggesting that there is an effective mass in the associated chiral modes. This subtle matter will be investigated in future work.
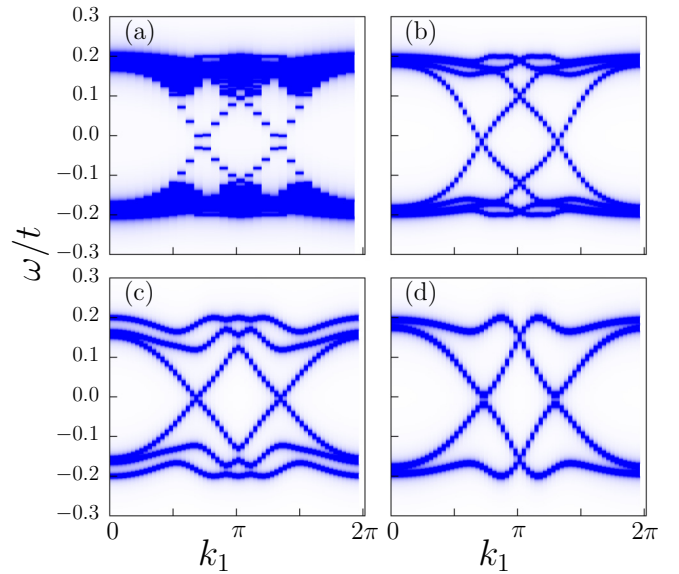

FIG. 9. One-particle spectral function $A(k_1, \omega)$ vs k_1 for various clusters, using PBC $\times$ OBC (PBC in the long direction). For all panels, we used broadening $\eta = 0.002t$ and energy resolution $d\omega = 0.001t$. Parameters for (a) are $\lambda = 0.3t$, $B = 0.2t$, and $\epsilon = 0.6t$, and cluster size 30 $\times$ 30. In (b) parameters are $\lambda = 0.3t$, $B = 0.2t$, and $\epsilon = 0.6t$, with cluster size 60 $\times$ 4. In (c), parameters are $\lambda = 0.7t$, $B = 0.2t$, and $\epsilon = 0.6t$, with cluster size 60 $\times$ 3. In (d), parameters are $\lambda = 0.5t$, $B = 0.2t$, and $\epsilon = 0.6t$, with cluster size 60 $\times$ 2.

B. Open boundary conditions in both directions

1. Edge currents in N × N system

As further test of the finite-size dice ribbons, in Fig. 10 we calculated the charge current for OBC along both directions, with both nonzero λ and B. First, we use a cluster mimicking two dimensions, with the same number of unit cells along both directions. In Fig. 10 edge currents develop for a 12 $\times$ 12 cluster, as expected. We confirmed the same for up to 30 $\times$ 30 clusters, but displaying the smaller system 12 $\times$ 12
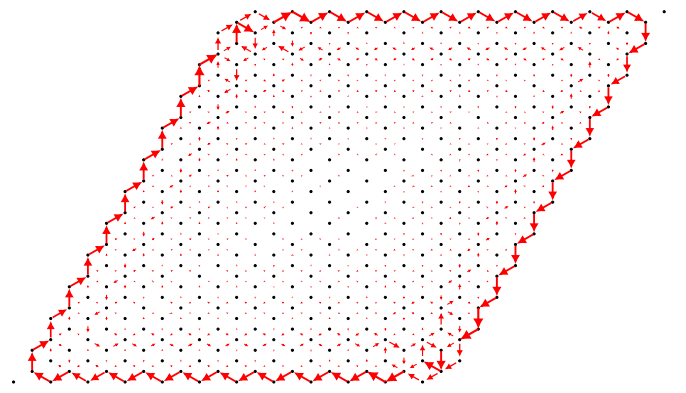

FIG. 10. Charge current calculated at each lattice bond on a 12 $\times$ 12 system with OBC $\times$ OBC boundary conditions, at $\lambda = 0.3t$, $B = 0.2t$, and $\epsilon = 0.6t$. The presence of edge currents is obvious to the eye. The intensity of the current is proportional to the length (and also to the width) of the arrows.
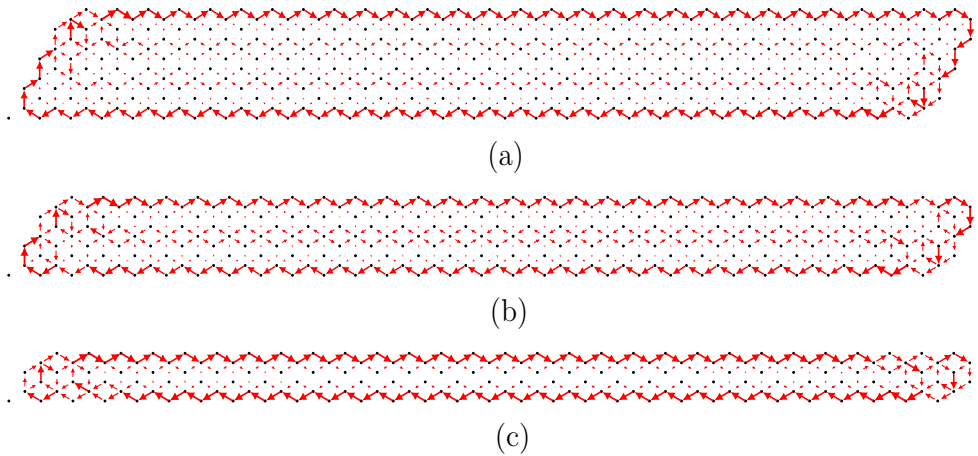
(a)

(b)

(c)

FIG. 11. Charge current calculated at each lattice bond for different ladder sizes. In (a) the system size is 30×4 while the parameters chosen are $\lambda = 0.3t$, $B = 0.2t$, and $\epsilon = 0.6t$. In (b) the system size is 30×3, with parameters $\lambda = 0.3t$, $B = 0.25t$, and $\epsilon = 0.6t$. In (c) the system size is 30×2 with parameters $\lambda = 0.1t$, $B = 0.4t$, and $\epsilon = 0.6t$. All plots are using boundary conditions OBC $\times$ OBC. Edge currents are present in the three ladders.

provides better clarity. The dangling sites of the OBC $\times$ OBC geometries have zero current due to current conservation. In fact, we confirmed explicitly charge conservation at every site. In the two vertices without dangling sites, where the current changes direction abruptly, this current extends more into the bulk than at the straight edges.

2. Edge currents in N × 4, N × 3, N × 2 dice ladders

For the 4-, 3-, and 2-leg dice ladders, results are similar as in the symmetric 12×12 cluster: in all cases there are sharply defined edge currents, see Fig. 11. As we reduce the number of legs we adjusted λ and B to better achieve the confinement of current to the edges. Without this adjustment, the edge currents moving left and right, along the two horizontal edges, develop an overlap because they have a finite width near the edge. However, even if in some regions of parameter space the edge currents are not as crisp as in Fig. 11 due to overlaps, in all cases the currents sense of rotation is the same and their existence is clear. In summary, all ladders behave similarly to planes when OBC conditions are used along both directions: in all cases edge currents develop.

Together with the presence of currents at the edges, we also observed the presence of charge related to in-gap states localized at the edges. Figure 12 shows the electronic density corresponding to the range of energies inside the gap opened by B between the two flat bands. As for the two-dimensional lattice, Fig. 12(a), for the dice ribbons, Figs. 12(b) to 12(d), the in-gap states generated by using OBC $\times$ OBC are indeed confined to be "edge states" as manifested by the edges' localization of charge.

3. Hall conductance

The Hall conductance was also calculated. Typically, σ_{xy} grows with increasing energy, starting from negative energy when the first flat band is reached. This is to be expected because of the nonzero value of C for the flat bands near zero energy in two dimensions. For PBC $\times$ PBC and after

entirely crossing the first lower flat band, σ_{xy} remains constant, and then it decreases when reaching the second band that has the same C but of opposite sign. For OBC $\times$ OBC or PBC $\times$ OBC, the edge states levels in between the flat bands makes σ_{xy} evolve more smoothly in value in between the flat bands, as opposed to having a plateau. However, overall
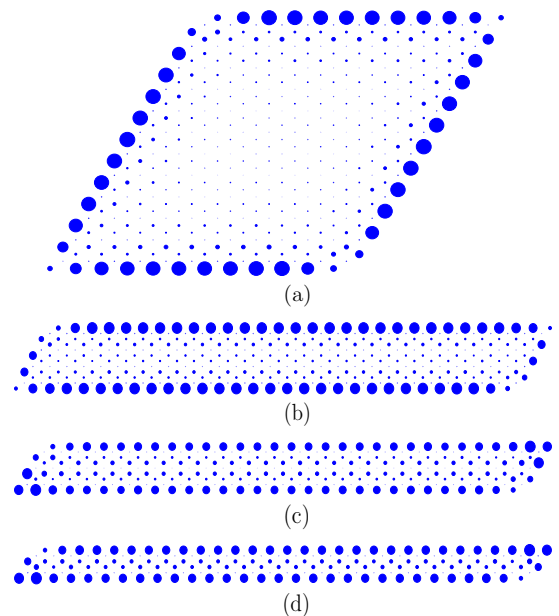

(a)

(b)

(c)

(d)

FIG. 12. Electronic density adding the contributions from all the "edge states" generated by using OBC $\times$ OBC—in between the two flat bands near zero energy—more specifically within the range $\Delta \omega = 0.2t$ from $\omega = -0.1t$ to $0.1t$. The radius of each circle is proportional to the density value. These states, that also generate the edge currents, are localized at the edge, as expected. Parameters used are as follows: (a) 12×12 cluster, $\lambda = 0.3t$, $B = 0.2t$, and $\epsilon = 0.6t$; (b) 30×4, $\lambda = 0.3t$, $B = 0.2t$, and $\epsilon = 0.6t$; (c) 30×3, $\lambda = 0.7t$, $B = 0.2t$, and $\epsilon = 0.6t$; (d) 30×2, $\lambda = 0.5t$, $B = 0.2t$, and $\epsilon = 0.6t$.

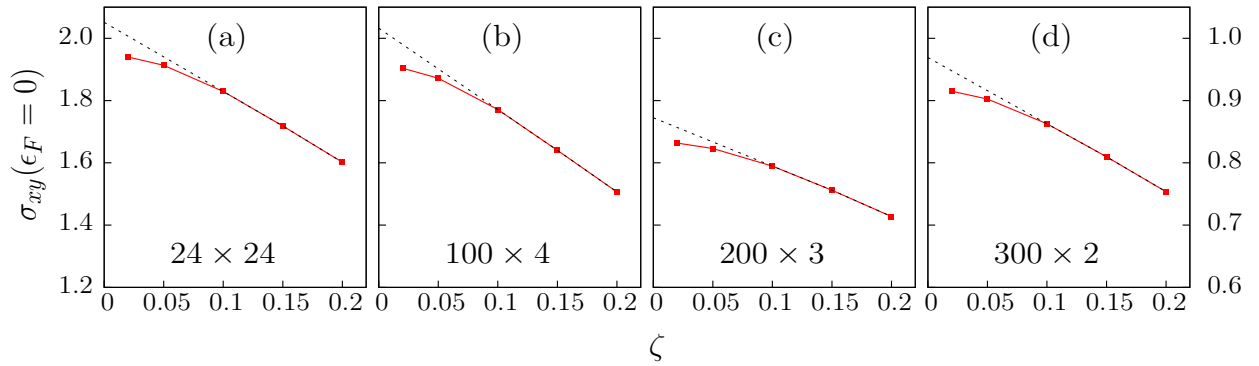FIG. 13. Hall conductance (σ_{xy}) at the Fermi level ($\epsilon_F = 0$) vs the relaxation parameter ζ for PBC × PBC clusters of sizes (a) 24 × 24, (b) 100 × 4, (c) 200 × 3, and (d) 300 × 2, all for the same parameters $\lambda = 0.3t$, $B = 0.2t$, and $\epsilon = 0.6t$. (a,b,c) share the vertical axis on the left, while (d) has its own vertical axis on the right. The extrapolation to zero broadening can be performed using all the red dots data or instead the dashed-line shown employing only broadenings above $0.1t$. The reason is that the systematic development of a negative curvature in the data, deviating from a straight line, could be a size or broadening effect. In panel (a) clearly both extrapolations via all the red dots or only using those leading to the dashed line suggest a convergence very close to the expected $C = 2$.

all the clusters studied, both the symmetric $N \times N$ and the dice ladders, share a qualitatively similar behavior in the Hall conductance. Note that our study of the Hall conductance is not with the goal of proposing specific experiments, but theoretically to observe how close the results for one-dimensional ladders resemble the two-dimensional results, where σ_{xy} is proportional to C.

With respect to the specific value reached at the central energy $\epsilon_F = 0$, for the 24 × 24 cluster and PBC × PBC the number is approximately 1.9, close to the expected 2. Size effects are to be expected and extrapolating to large N, we conclude that C for the $N \times N$ cluster is indeed very close to 2 within our accuracy. For the dice ladders, systematically the zero energy Hall conductance is smaller, although they are all qualitatively similar. In all cases, the $\epsilon_F = 0$ value is larger than 1.

In Fig. 13 the Fermi-energy Hall conductance is shown versus broadening for PBC × PBC where size effects are less severe. In the caption, two alternative extrapolations to zero broadening are discussed. For the 24 × 24, it appears that $C = 2$ is a solid conclusion, in agreement with expectations. For the 4-leg ladder, results also suggest $C \sim 2$. As explained before, we do not expect C to behave exactly similarly in dice ribbons as in two-dimensional dice lattices, but the results shown are sufficient to illustrate that the 4-leg ladder is virtually identical to the two-dimensional system. However, for the 3-leg dice ladders, deviations are pronounced and it seems unlikely C will extrapolate to 2. Similarly, the case of the 2-leg ladder is even more pronounced, with a C close to 1. For 3- and 2-leg ladders, the edge currents moving in opposite directions may start overlapping, distorting the effects found in planes. Yet, all of the dice lattices we studied have systematic behavior similar to one another.

V. CORRELATION EFFECTS

In this section we address the second primary goal of this paper, the effect of Hubbard correlations U. As explained before, considering correlation effects in two dimensions is difficult without using severe approximations. For this reason

in the first portion of this paper we verified that ribbons of the dice lattice ("ladders") maintain the essential properties of the two-dimensional version, such as flat bands. In this section now we introduce correlation effects U using the accurate Lanczos and DMRG techniques. For the later method we employ the 8 × 2 cluster. Note that this cluster has a total of 48 sites and in the short direction there are six rows of sites. In spite of this complexity, it can still be studied with DMRG. Other dice ladders like $N \times 3$ are more computationally challenging and its analysis will be attempted in future work. However, the $N \times 2$ cluster is here shown to be sufficient to illustrate the development of nontrivial magnetic order in the dice systems with increasing U.

First, consider the effect of U on the DOS at $B = 0$, particularly the flat bands, using the Lanczos technique on a 2 × 2 exactly solved cluster (12 sites). Results are in Fig. 14,
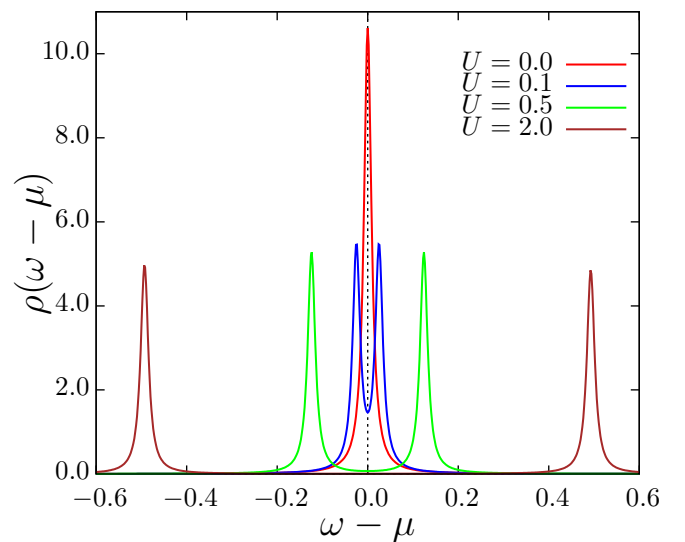

FIG. 14. DOS of a 2 × 2 cluster (12 sites) studied exactly with Lanczos for various values of U, using PBC × PBC. Shown are results for $\lambda = 0.2t$, $\epsilon = 0.6t$, $B = 0$, $\eta = 0.01t$, and $d\omega = 0.002t$.
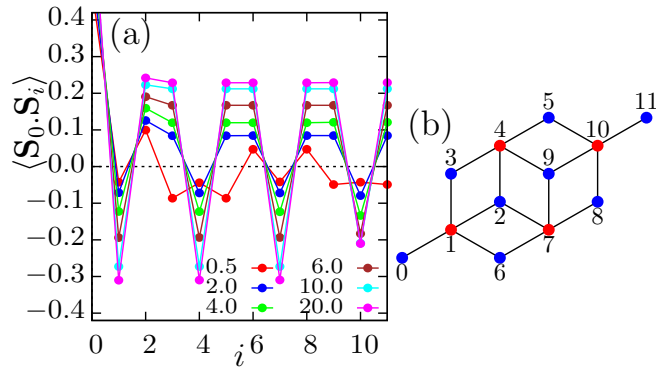
FIG. 15. (a) Real-space spin-spin correlation between a reference site 0 and all other sites, labeled as shown in panel (b) using the "snake" geometry of DMRG. We use a 2×2 cluster studied with Lanczos for various U's [values indicated as inset in panel (a)], PBC $\times$ PBC, $\lambda = 0.2t$, $\epsilon = 0.6t$, and $B = 0$.

focusing on the energy range near the flat bands of Fig. 7. From these DOS results, it is clear that U splits the flat bands similarly as a magnetic field does, with a gap growing with U. As explained below, the qualitative reason is that the spin state that develops as U increases has ferrimagnetic tendencies, and the net global magnetization of such state qualitatively resembles an external magnetic field.

In Fig. 15(a), the spin-spin correlations measured exactly using the Lanczos technique are shown for a small cluster 2×2 (12 sites), parametric with U. Site labels are in Fig. 15(b). As the Hubbard repulsion grows, the magnetic order (the strength of the spin-spin correlations) grows. The pattern shown corresponds to ferrimagnetic order, at least for $U = 2$ or larger, because the number of spin correlations that are positive is double the number that are negative, with a different spin orientation for the coordination 3 and 6 sites spins. At $U = 0.5$ the spin correlations are more erratic, but still there is an unbalance between positive and negative. Typically, size effects are more severe at small U, but the ferrimagnetic pattern at $U = 2$ or larger is robust.

The Lanczos results are in excellent agreement with the spin-spin correlations obtained using DMRG employing a larger 8×2 cluster, as shown in Fig. 16(a). These results are displayed using the "snake" geometry where all 48 sites are arranged in a one-dimensional structure, commonly used in DMRG, see Fig. 16(b). The fact that for each negative value of the correlation there are two positives is again indicative of the ferrimagnetic order, with a net magnetic moment, as in the Lanczos study. Note that for $U = 0.5$ the ferrimagnetic pattern is clear, suggesting that the erratic $U = 0.5$ results of Lanczos are a size effect.

Thus, overall the conclusion is that accurate numerical techniques on dice ladders indicate that (1) ferrimagnetic order develops, and (2) the split of the flat bands does not require an external magnetic field but correlation effects can produce related effects via ferrimagnetism. This magnetic state is in agreement with studies of the spin-1/2 Heisenberg model on a dice lattice [32]. However, our results are not consistent with those obtained with the Hartree approximation when including the Hubbard U that predicted ferromagnetic order [10], instead of ferrimagnetic, illustrating the value of
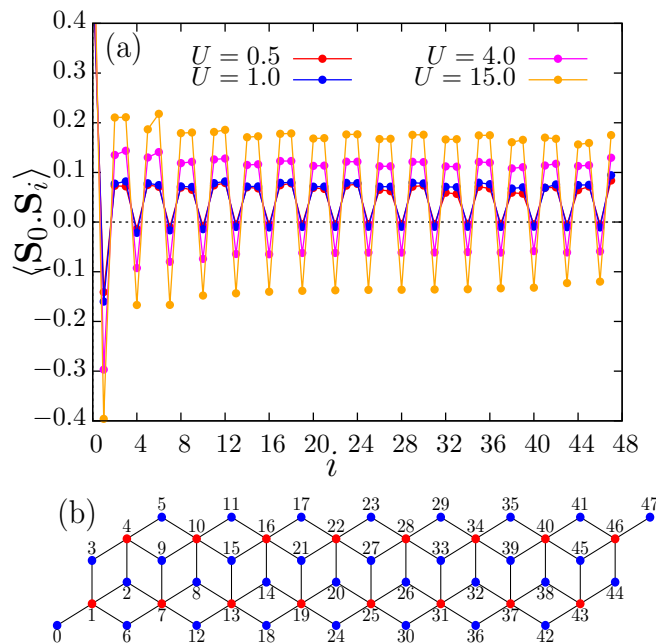

FIG. 16. (a) Real-space spin-spin correlation between a reference site 0 and all other sites of an 8×2 cluster (48 sites total) for different values of interaction U. Results shown were obtained with DMRG, and the cluster has OBC in the long direction. Here $\lambda = 0.2t$, $\epsilon = 0.6t$, and $B = 0$. Site labels are in panel (b).
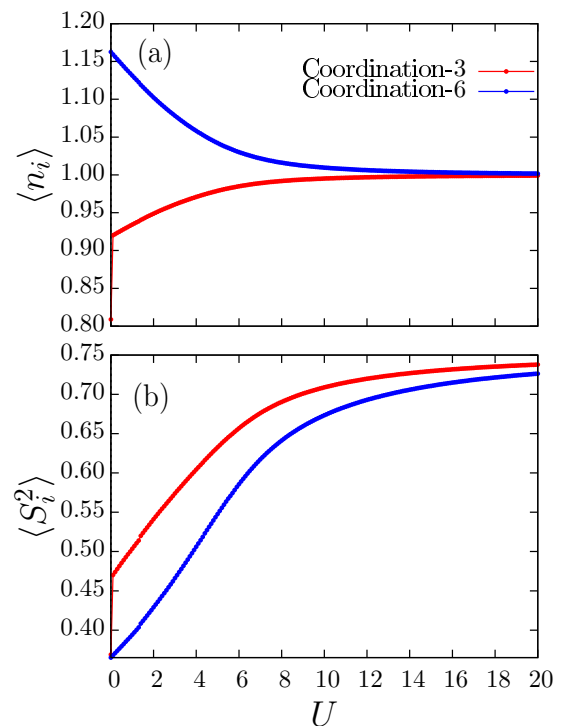

FIG. 17. (a) Local charge density and (b) average local moment squared for coordination-3 and coordination-6 sites in a 2×2 PBC $\times$ PBC system via Lanczos. The plots are for $\lambda = 0.2t$, $\epsilon = 0.6t$, and $B = 0$.
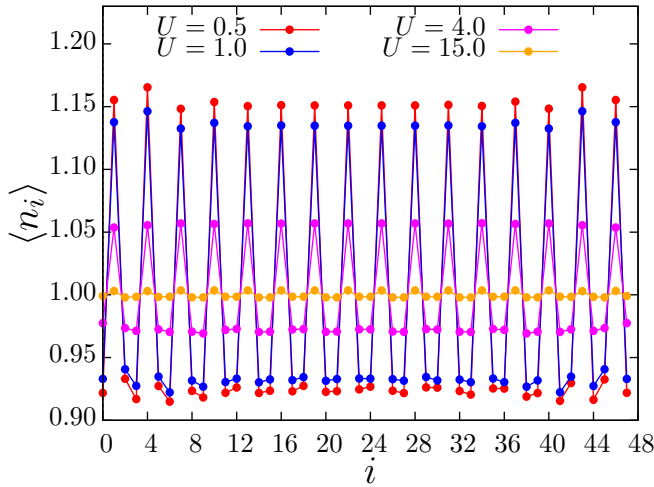
FIG. 18. Local electronic density for the 8×2 cluster (48 sites) obtained via DMRG for different values of interaction U. The plots are for $\lambda = 0.2t$, $\epsilon = 0.6t$, and $B = 0$, using the "snake" geometry of DMRG.

carrying out calculations with techniques such as Lanczos and DMRG.

For completeness, we also show the Lanczos local charge density in Fig. 17(a). As intuitively expected, the probability of double occupancy is strongly suppressed with increasing U and asymptotically the density approaches 1. Simultaneously with the local charge reaching 1, the local spin reaches 1/2 as shown in Fig. 17(b) where at large U the squared-spin expectation value converges to $1/2(1 + 1/2) = 0.75$. All this occurs similarly for coordination 3 and 6 sites, even though the weak and intermediate U coupling values are slightly different.

Similarly as with Lanczos, using DMRG we also studied the electronic density. The results in Fig. 18, using the "snake" geometry, confirm that with increasing U the local densities converge to 1.

VI. CONCLUSION

We studied the dice lattice when geometrically reduced from the standard two-dimensional geometry to quasi-one-dimensional ribbons that we call ladders. Because we aim to reach the community of experts in correlated electronic systems, the term "ladders" was often used instead of ribbons by analogy to the physical systems widely studied in other contexts, such as high critical temperature superconductors [33–40]. The Hamiltonian used when neglecting Hubbard repulsion is the same as in Ref. [10], with a tight-binding term, Rashba spin-orbit coupling, on-site energies, and an external magnetic field. In addition, we incorporated the effect of Hubbard interactions in the $N \times 2$ ladders, using Lanczos and DMRG methods.

Our main results are two fold.

(1) We showed that the geometrical transition from planes to ribbons does not alter the basic properties of the dice lattice. We arrived to this conclusion focusing on several nontrivial quantities of relevance in two dimensions, such as the flat bands near the Fermi level, the edge currents when using OBC, the localized charge at the edges near zero energy in

the one-particle spectral function also when using OBC, and a nonzero Hall conductance. The main conclusion of this first portion of our effort is that all systems studied, more importantly the 2-leg ladder that can be studied with DMRG including Hubbard U, display common properties suggesting that their qualitative behavior is similar. Remarkably, the original localized states that create the flat bands are present in all the systems studied here, suggesting their localization length is very small, a result that could not be predicted *a priori*.

(2) In the second portion of this paper, for the first time we introduced and studied the effect of Hubbard correlations U in dice systems using Lanczos and DMRG techniques, for the case of the $N \times 2$ ladder. We show that the dice systems generate ferrimagnetic order with increasing U and the flat bands split in the correlated systems without the need of introducing an external magnetic field. Our results improve over previous mean-field efforts that reported ferromagnetic order instead.

This effort paves the way towards an in-depth study of correlation effects in dice systems. For example, for the 2-leg dice ladder, the DOS can be analyzed in the entire U-λ plane. Using DMRG such work will require considerable computer-time resources but we estimate the effort is doable in the near future. We also can study how the ferrimagnetic order evolves increasing λ, as well as the effects of U on edge currents. The future DMRG studies will require OBC along the long direction, as technically needed in DMRG, but the short direction can be OBC or PBC. All these exciting results on the challenging effects of incorporating both U and λ in dice systems will be presented in the near future.

APPENDIX A: CHARGE CURRENT OPERATORS

From the kinetic term of the Hamiltonian and using the continuity equation for the charge, the following current operators were derived [41]:

$$J^{\mathrm{K}}_{j \to i_p} = J_{j \to i_p, \uparrow \to \uparrow} + J_{j \to i_p, \downarrow \to \downarrow}, \tag{A1}$$

where i_p's are the six neighboring sites of site j as shown in Fig. 19 with $p = 1, \ldots, 6$. The current operator used above is defined as $J_{j \to i_p, \sigma \to \sigma} = -\mathrm{i}t(c^{\dagger}_{i_p,\sigma} c_{j,\sigma} - \mathrm{H.c.})$.

Similarly, from the SOC term of the Hamiltonian, the following charge current operators were derived:

$$J^{\mathrm{SO}}_{j \to i_p} = J_{j \to i_p, \uparrow \to \downarrow} + J_{j \to i_p, \downarrow \to \uparrow}, \tag{A2}$$

where $J_{j \to i_p, \sigma \to \sigma'} = \lambda[c^{\dagger}_{i_p,\sigma'}(\hat{D}_{i_p j}.\bar{\tau})_{\sigma'\sigma} c_{j,\sigma} + \mathrm{H.c.}]$, and here $\sigma \neq \sigma'$.

The total charge current from site j to one of the neighboring sites i_p is

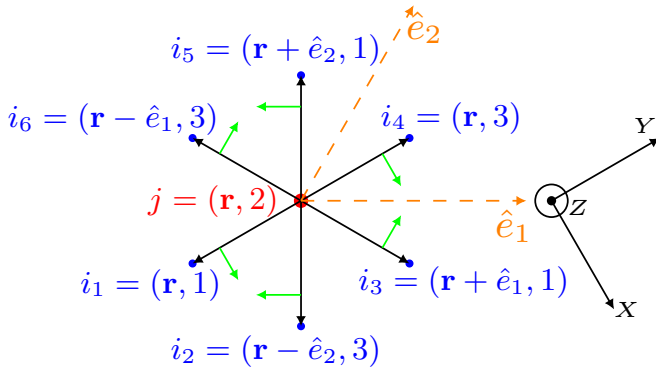$$J^{c}_{j \to i_p} = J^{K}_{j \to i_p} + J^{\mathrm{SOC}}_{j \to i_p}. \tag{A3}$$

FIG. 19. Rashba-SOC lattice connections from the six-coordination site $j = (\mathbf{r}, 2)$, as an example. The green arrows depict the SOC vectors $\hat{D}_{ij}$ for the bonds connected to j. $\hat{e}_1$ and $\hat{e}_2$ are the lattice unit vectors. 1, 2, and 3 are the site labels within a unit cell $\mathbf{r}$. Following [10], X, Y, and Z are the axes of the spin space used for the Rashba connections: the Y direction is parallel to the line from $(\mathbf{r},2)$ to $(\mathbf{r},3)$, and the X direction is perpendicular.

These definitions of charge currents satisfy the conservation property (both locally and globally).

APPENDIX B: CHERN NUMBER

The Chern number for the nth band is defined in the continuum as

$$C_n = \frac{1}{2\pi i} \int_{T^2} F_{12}(\mathbf{k}) d\mathbf{k}, \tag{B1}$$

where $F_{12}(\mathbf{k}) = \partial_1 A_2(\mathbf{k}) - \partial_2 A_1(\mathbf{k})$ is the Berry curvature, and $A_\mu(\mathbf{k}) = \langle u_{n,\mathbf{k}} | \partial_\mu | u_{n,\mathbf{k}} \rangle$ is the Berry connection. T^2 is the surface of a Torus formed by considering periodic boundary condition (PBC) in both the $\hat{e}_1$ and $\hat{e}_2$ directions. $\partial_\mu \equiv \partial/\partial k_\mu$ is the partial derivative with respect to momentum k_1 and k_2 along the $\hat{e}_1$ and $\hat{e}_2$ directions, respectively.

For lattice calculations, the above equations cannot be used unless we find Bloch functions "$\langle \mathbf{r}, \alpha, \sigma | u_{n,\mathbf{k}} \rangle$" in a real-space basis. Since our Hamiltonian is translationally invariant, the set of Bloch states $\{\langle \mathbf{r}, \alpha, \sigma | \Psi_{n,\mathbf{k}} \rangle\}$ are eigenstates of the Hamiltonian, where $\Psi_{n,\mathbf{k}}(\mathbf{r}, \alpha, \sigma) = \langle \mathbf{r}, \alpha, \sigma | \Psi_{n,\mathbf{k}} \rangle = e^{i\mathbf{k}\cdot\mathbf{r}} u_{n,\mathbf{k}}(\mathbf{r}, \alpha, \sigma)$, and in the second quantization $|\mathbf{r}, \alpha, \sigma \rangle = c^\dagger_{\mathbf{r},\alpha,\sigma} |0\rangle$. Note that the set $\{\langle \mathbf{r}, \alpha, \sigma | \Psi_{n,\mathbf{k}} \rangle\}$ are orthogonal to each other but not necessarily the set $\{\langle \mathbf{r}, \alpha, \sigma | u_{n,\mathbf{k}} \rangle\}$ which explains why the Berry connections are (always) nonzero.

Because our computational calculation was performed primarily in a real-space basis, the eigenstates we obtain are, in general, a superposition of all the Bloch states with the same energy, see Fig. 20. For this reason, we cannot directly use the eigenstates calculated from the diagonalization computer code to find the Chern number.

To solve this issue, consider a computer-generated real-space eigenstate $|m\rangle$ with energy E_m. This state is a linear combination of the real-space site basis, i.e., $|m\rangle = \sum_{\mathbf{r},\alpha,\sigma} C_{\mathbf{r},\alpha,\sigma}(m) |\mathbf{r}, \alpha, \sigma\rangle$, where $C_{\mathbf{r},\alpha,\sigma}(m) = \langle \mathbf{r}, \alpha, \sigma | m \rangle$ are the coefficients of the transformation matrix from site basis to the real-space eigenstate of the Hamiltonian.
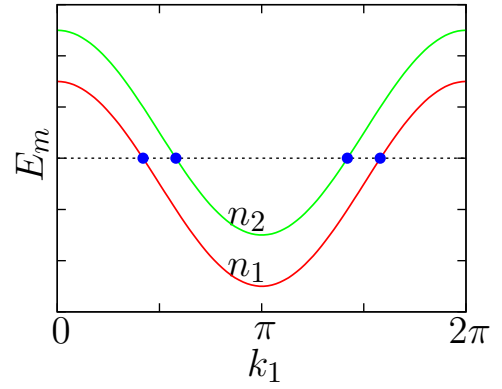

FIG. 20. E_m vs k_1 sketch illustrating how we computed $\langle \mathbf{r}, \alpha, \sigma | \Psi_{n,\mathbf{k}} \rangle$ between two nondegenerate nontouching bands (points in blue are explained in the text).

As expressed above, $|m\rangle$ can also be written as a superposition of all the Bloch states $|\Psi_{n,\mathbf{k}}\rangle$ with the same energy (see Fig. 20) as $|m\rangle = \sum_{n,\mathbf{k}} \Gamma^n_\mathbf{k}(m) |\Psi_{n,\mathbf{k}}\rangle$, where $\Gamma^n_\mathbf{k}(m) = \langle \Psi_{n,\mathbf{k}} | m \rangle$ are the transformation coefficients from Bloch states to real-space eigenstates. From the above equations and considering that $u_{n,\mathbf{k}}(\mathbf{r}, \alpha, \sigma) = \langle \mathbf{r}, \alpha, \sigma | u_{n,\mathbf{k}} \rangle$ are repeated between unit cells, i.e., $u_{n,\mathbf{k}}(\mathbf{r}, \alpha, \sigma) = u_{n,\mathbf{k}}(\mathbf{r} + \mathbf{r}', \alpha, \sigma)$, we calculate: $\sum_{\mathbf{r}'} \langle \mathbf{r} + \mathbf{r}', \alpha, \sigma | m \rangle e^{-i\mathbf{k}\cdot\mathbf{r}'} =$

$$\sum_{n,\mathbf{k}',\mathbf{r}'} \Gamma^n_{\mathbf{k}'}(m) \langle \mathbf{r} + \mathbf{r}', \alpha, \sigma | \Psi_{n,\mathbf{k}'} \rangle e^{-i\mathbf{k}\cdot\mathbf{r}'}$$

$$= \sum_{n,\mathbf{k}',\mathbf{r}'} \Gamma^n_{\mathbf{k}'}(m) e^{i\mathbf{k}'\cdot(\mathbf{r}'+\mathbf{r})} \langle \mathbf{r} + \mathbf{r}', \alpha, \sigma | u_{n,\mathbf{k}'} \rangle e^{-i\mathbf{k}\cdot\mathbf{r}'}$$

$$= \sum_{n,\mathbf{k}',\mathbf{r}'} \Gamma^n_{\mathbf{k}'}(m) e^{i\mathbf{k}'\cdot(\mathbf{r}'+\mathbf{r})} e^{-i\mathbf{k}\cdot\mathbf{r}'} \langle \mathbf{r}, \alpha, \sigma | u_{n,\mathbf{k}'} \rangle$$

$$= V \sum_n \Gamma^n_\mathbf{k}(m) e^{i\mathbf{k}\cdot\mathbf{r}} \langle \mathbf{r}, \alpha, \sigma | u_{n,\mathbf{k}} \rangle$$

$$= V \sum_n \Gamma^n_\mathbf{k}(m) \langle \mathbf{r}, \alpha, \sigma | \Psi_{n,\mathbf{k}} \rangle, \tag{B2}$$

where it must be understood that $|\mathbf{r} + \mathbf{r}', \alpha, \sigma \rangle = c^\dagger_{\mathbf{r}+\mathbf{r}',\alpha,\sigma} |0\rangle$, and V is the volume of the system. We know that Chern numbers are well defined only for nonintersecting energy bands. In our case, with the addition of the Rashba-SOC and the Zeeman field (B) we fulfill this condition. From this physical argument, illustrated in Fig. 20, we know that for fixed momentum $\mathbf{k}$ and energy E_m, only one value of $\Gamma^n_\mathbf{k}(m)$ is nonzero for a specific band n. Thus, we can write Eq. (B2) as

$$\sum_{\mathbf{r}'} \langle \mathbf{r} + \mathbf{r}', \alpha, \sigma | m \rangle e^{-i\mathbf{k}\cdot\mathbf{r}'} = V \Gamma^n_\mathbf{k}(m) \langle \mathbf{r}, \alpha, \sigma | \Psi_{n,\mathbf{k}} \rangle. \tag{B3}$$

Of course we do not know the specific value of $\Gamma^n_\mathbf{k}(m)$, but Eq. (B3) implies that for each individual band n, $\langle \mathbf{r}, \alpha, \sigma | \Psi_{n,\mathbf{k}} \rangle \propto \sum_{\mathbf{r}'} \langle \mathbf{r} + \mathbf{r}', \alpha, \sigma | m \rangle e^{-i\mathbf{k}\cdot\mathbf{r}'}$, so by calculating $\sum_{\mathbf{r}'} \langle \mathbf{r} + \mathbf{r}', \alpha, \sigma | m \rangle e^{-i\mathbf{k}\cdot\mathbf{r}'}$ and normalizing it, the Bloch states $(\Psi_{n,\mathbf{k}}(\mathbf{r}, \alpha, \sigma) = \langle \mathbf{r}, \alpha, \sigma | \Psi_{n,\mathbf{k}} \rangle)$ can be obtained in real space for band n. After calculating this Bloch states, now $u_{n,\mathbf{k}}(\mathbf{r}, \alpha, \sigma)$ can be obtained using $\langle \mathbf{r}, \alpha, \sigma | u_{n,\mathbf{k}} \rangle = e^{-i\mathbf{k}\cdot\mathbf{r}} \langle \mathbf{r}, \alpha, \sigma | \Psi_{n,\mathbf{k}} \rangle$, which can directly be used for the calculation of the Chern number.
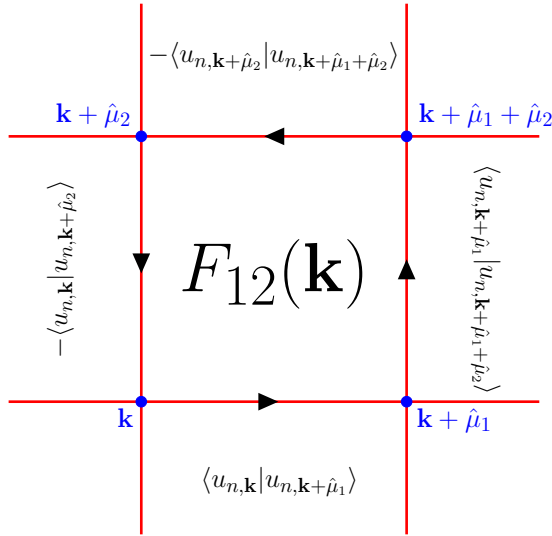
FIG. 21. Pictorial representation of the flux variable $F_{12}(\mathbf{k})$ in a k-space plaquette.

Once the Bloch functions are found, we follow the method of Fukui *et al.* [43], to calculate the Chern number for a discrete lattice. We first compute the $U(1)$ link variables $U_\mu(\mathbf{k}) = \langle u_{n,\mathbf{k}}(\mathbf{r}, \alpha, \sigma) | u_{n,\mathbf{k}+\hat{\mu}}(\mathbf{r}, \alpha, \sigma) \rangle / \| \langle u_{n,\mathbf{k}}(\mathbf{r}, \alpha, \sigma) | u_{n,\mathbf{k}+\hat{\mu}}(\mathbf{r}, \alpha, \sigma) \rangle \|$ as defined in their paper ($\hat{\mu}$ is a vector along the directions of the lattice vectors $\hat{e}_1$ and $\hat{e}_2$ with magnitude $2\pi / N_\mu$), from the Bloch functions evaluated above. Then, we calculate the discretized lattice field strength $F_{12}(\mathbf{k})$ as

$$F_{12}(\mathbf{k}) = \partial_1 A_2(\mathbf{k}) - \partial_2 A_1(\mathbf{k})$$
$$\approx A_2(\mathbf{k} + \hat{\mu}_1) - A_2(\mathbf{k}) - A_1(\mathbf{k} + \hat{\mu}_2) + A_1(\mathbf{k}),$$
(B4)

where *forward* discretization of ∂_μ was used. Under this approximation, for example,

$$A_1(\mathbf{k}) \approx \langle u_{n,\mathbf{k}} | u_{n,\mathbf{k}+\hat{\mu}_1} \rangle - \langle u_{n,\mathbf{k}} | u_{n,\mathbf{k}} \rangle.$$
(B5)

Assuming that all $\{|u_{n,\mathbf{k}}\rangle\}$ are normalized to 1, it can be shown that

$$F_{12}(\mathbf{k}) \approx \langle u_{n,\mathbf{k}+\hat{\mu}_1} | u_{n,\mathbf{k}+\hat{\mu}_1+\hat{\mu}_2} \rangle - \langle u_{n,\mathbf{k}} | u_{n,\mathbf{k}+\hat{\mu}_2} \rangle$$
$$- \langle u_{n,\mathbf{k}+\hat{\mu}_2} | u_{n,\mathbf{k}+\hat{\mu}_1+\hat{\mu}_2} \rangle + \langle u_{n,\mathbf{k}} | u_{n,\mathbf{k}+\hat{\mu}_1} \rangle.$$
(B6)

Pictorially, each of these individual terms can be imagined by placing them at the links of a discretized Brillouin zone, as shown in Fig. 21. Moreover, the sign gives a sense of circulation. $F_{12}(\mathbf{k})$ then becomes a *flux* variable around an elementary plaquette of the k-space lattice. Then, following the directions [43] to calculate the lattice field strength $\tilde{F}_{12}(\mathbf{k}) = \ln [U_1(\mathbf{k})U_2(\mathbf{k} + \hat{\mu}_1)U_1(\mathbf{k} + \hat{\mu}_2)^{-1}U_2(\mathbf{k})^{-1}]$, we can compute the Chern number associated with the nth band as

$$C_n = \frac{1}{2\pi i} \sum_{\mathbf{k}} \tilde{F}_{12}(\mathbf{k}).$$
(B7)

Note that the magnitude of the quantities inside the lattice field strength $\tilde{F}_{12}(\mathbf{k})$ is always 1 and thus $-i\pi < \tilde{F}_{12}(\mathbf{k}) \leqslant i\pi$.

Following this momentum-space procedure, we calculated the Chern number for the $N \times N$ clusters, with focus on the flat band below the Fermi level. The results were clearly equal to 2 (not shown). A result $C \approx 2$ was obtained for the $N \times 4$ ladder, confirming that these two systems are, in practice, virtually identical. For the case of 3-leg ladders, however, our results seem to converge to a smaller C, in agreement with the deviations from the two observed in Fig. 13(c). For 2-leg ladders, the calculation is not possible due to the trivial cancellations arising from the availability of only two momenta along the short direction. Nevertheless, although using σ_{xy} and real-space edge currents is more reliable, the momentum-space method outlined in this Appendix provides results compatible with those in real space.

[1] F. D. M. Haldane, Phys. Rev. Lett. **61**, 2015 (1988).

[2] M. Z. Hasan and C. L. Kane, Rev. Mod. Phys. **82**, 3045 (2010).

[3] J. E. Moore, Nature **464**, 194 (2010).

[4] X. L. Qi and S. C. Zhang, Rev. Mod. Phys. **83**, 1057 (2011).

[5] E. Tang, J. W. Mei, and X. G. Wen, Phys. Rev. Lett. **106**, 236802 (2011).

[6] T. Neupert, L. Santos, C. Chamon, and C. Mudry, Phys. Rev. Lett. **106**, 236804 (2011).

[7] X. Hu, M. Kargarian, and G. A. Fiete, Phys. Rev. B **84**, 155116 (2011).

[8] C. Weeks and M. Franz, Phys. Rev. B **85**, 041104(R) (2012).

[9] D. N. Sheng, Z. C. Gu, K. Sun, and L. Sheng, Nat. Commun. **2**, 389 (2011).

[10] F. Wang and Y. Ran, Phys. Rev. B **84**, 241103(R) (2011).

[11] For earlier work on dice lattices in the presence of a magnetic field without Rashba term see J. Vidal, R. Mosseri, and B. Douçot, Phys. Rev. Lett. **81**, 5888 (1998); J. Vidal, P. Butaud, B. Douçot, and R. Mosseri, Phys. Rev. B **64**, 155306 (2001); See also B. Pal and K. Saha, *ibid.* **97**, 195101 (2018); E. V. Gorbar, V. P. Gusynin, and D. O. Oriekhov, *ibid.* **99**, 155124 (2019); B. Dey and T. K. Ghosh, *ibid.* **99**, 205429 (2019).

[12] A. A. Burkov and E. Demler, Phys. Rev. Lett. **96**, 180406 (2006).

[13] M. Rizzi, V. Cataudella, and R. Fazio, Phys. Rev. B **73**, 144511 (2006).

[14] D. Bercioux, D. F. Urban, H. Grabert, and W. Häusler, Phys. Rev. A **80**, 063603 (2009).

[15] For other systems with Chern number 2 or higher see Z. Liu, E. J. Bergholtz, H. Fan, and A. M. Laüchli, Phys. Rev. Lett. **109**, 186805 (2012); A. M. Cook and A. Paramekanti, *ibid.* **113**, 077203 (2014), and references therein.

[16] For a recent review see S. Okamoto and D. Xiao, J. Phys. Soc. Jpn. **87**, 041006 (2018), and references therein.

[17] E. Illes, J. P. Carbotte, and E. J. Nicol, Phys. Rev. B **92**, 245410 (2015).

[18] E. Illes and E. J. Nicol, Phys. Rev. B **94**, 125435 (2016).

[19] SK Firoz Islam and P. Dutta, Phys. Rev. B **96**, 045418 (2017).

[20] B. Dey and T. K. Ghosh, Phys. Rev. B **98**, 075422 (2018).

[21] B. Dóra, I. F. Herbut, and R. Moessner, Phys. Rev. B **90**, 045310 (2014).

[22] G. Möller and N. R. Cooper, Phys. Rev. Lett. **108**, 045306 (2012).

[23] T. Andrijauskas, E. Anisimovas, M. Račiūnas, A. Mekys, V. Kudriašov, I. B. Spielman, and G. Juzeliūnas, Phys. Rev. A **92**, 033617 (2015).

[24] D. Doennig, W. E. Pickett, and R. Pentcheva, Phys. Rev. Lett. **111**, 126804 (2013).

[25] R. Rawl, M. Lee, E. S. Choi, G. Li, K. W. Chen, R. Baumbach, C. R. dela Cruz, J. Ma, and H. D. Zhou, Phys. Rev. B **95**, 174438 (2017).

[26] T. Cao, F-Z. Zhao, and S. G. Louie, Phys. Rev. Lett. **119**, 076401 (2017).

[27] Although not cylindrical ladders as in our publication, the study of nontrivial Berry phase effects in one-dimensional models with flat bands was discussed by H. Guo, S.-Q. Shen, and S. Feng, Phys. Rev. B **86**, 085124 (2012).

[28] The optical response of nanoribbons within the α-T_3 model was also addressed recently by Y.-R. Chen, Y. Xu, J. Wang, J.-F. Liu, and Z. Ma, Phys. Rev. B **99**, 045420 (2019).

[29] For a recent review see S. Rachel, Rep. Prog. Phys. **81**, 116501 (2018), and references therein.

[30] E. Dagotto, Rev. Mod. Phys. **66**, 763 (1994).

[31] U. Schollwöck, Ann. Phys. (NY) **326**, 96 (2011).

[32] H. Nakano and T. Sakai, J. Phys. Soc. Jpn. **86**, 063702 (2017).

[33] H. Takahashi, A. Sugimoto, Y. Nambu, T. Yamauchi, Y. Hirata, T. Kawakami, M. Avdeev, K. Matsubayashi, F. Du, C. Kawashima, H. Soeda, S. Nakano, Y. Uwatoko, Y. Ueda, T. J. Sato, and K. Ohgushi, Nat. Mater. **14**, 1008 (2015).

[34] N. D. Patel, A. Nocera, G. Alvarez, R. Arita, A. Moreo, and E. Dagotto, Phys. Rev. B **94**, 075119 (2016).

[35] Q. Luo, A. Nicholson, J. Rincón, S. Liang, J. Riera, G. Alvarez, L. Wang, W. Ku, G. D. Samolyuk, A. Moreo, and E. Dagotto, Phys. Rev. B **87**, 024404 (2013).

[36] M. Mourigal, S. Wu, M. B. Stone, J. R. Neilson, J. M. Caron, T. M. McQueen, and C. L. Broholm, Phys. Rev. Lett. **115**, 047401 (2015).

[37] J. Herbrych, N. Kaushal, A. Nocera, G. Alvarez, A. Moreo, and E. Dagotto, Nat. Commun. **9**, 3736 (2018).

[38] E. Dagotto, J. A. Riera, and D. J. Scalapino, Phys. Rev. B **45**, 5744(R) (1992).

[39] E. Dagotto and T. M. Rice, Science **271**, 618 (1996).

[40] M. Uehara, T. Nagata, J. Akimitsu, H. Takahashi, N. Môri, and K. Kinoshita, J. Phys. Soc. Jpn. **65**, 2764 (1996).

[41] J. A. Riera, arXiv:1802.01035.

[42] N. Mohanta, E. Dagotto, and S. Okamoto, Phys. Rev. B **100**, 064429 (2019).

[43] T. Fukui, Y. Hatsugai, and H. Suzuki, J. Phys. Soc. Jpn. **74**, 1674 (2005).